Journal of Alloys and Compounds 861 (2021) 158620

Contents lists available at ScienceDirect

Journal of Alloys and Compounds

journal homepage: www.elsevier.com/locate/jalcom

Cd-doped ZnO nanoparticles: An experimental and first-principles DFT studies

E. Ozugurlu

Istanbul Technical University, Department of Mathematics, 34469 Maslak, Istanbul, Turkey

ARTICLE INFO

Article history:
Received 11 December 2020
Received in revised form 30 December 2020
Accepted 31 December 2020
Available online 6 January 2021

Keywords:
Sol–gel
Williamson–Hall
Stress
Microstrain
DFT

ABSTRACT

The sol–gel method was used for $Zn_{1-x}Cd_xO$ nanoparticles with various concentrations (x = 0.01, 0.02, 0.03, 0.04, 0.05, 0.1, 0.2, and 0.3). This work aimed to compare the estimated stress, strain, and crystallite size of $Zn_{1-x}Cd_xO$ nanoparticles using the Williamson–Hall method with the help of the least-squares method for various Cd concentrations with the Debye–Scherrer formula whose level of accuracy was found to be sufficiently comprehensive for this study. The linear regression model was also analyzed statistically and it was shown that our model was very good for 5% of Cd, where the *p*-values were 0.0018, 0.0202, and 0.0061 for the UDM, USDM, and UDEDM, respectively. According to the density functional theory (DFT) calculations within GGA and GGA+U based on experimental structural data deducing that high band-gap tuned via CBM instead of VB states and increasing Cd amount let band-gap lowered. A redshift was observed according to absorption spectra of the visible region which is more obvious by increasing Cd amount. In addition, one can conclude that band-gap is decreased when crystalline size is reduced through increasing guest concentration. The X-ray diffraction method was used for the structural analysis of all nanoparticles. Up to $x < 0.02$, Cd replaced Zn and yielded ZnO single phase; while for $x \geq 0.02$, two phases (ZnO and CdO) emerged. To determine surface morphology, particle size, and shapes of the nanoparticles, the SEM technique was employed and the EDS was utilized for the elemental compositions of the nanoparticles. It was observed that the ZnCdO nanoparticles had a hexagonal wurtzite structure. Moreover, the crystallite size, microstrain, and stress values became maximum for the $Zn_{0.95}Cd_{0.05}O$ sample.

1. Introduction

Zinc oxide (ZnO) has been playing a crucial role in solar cells, medical devices, the auto industry, semiconductors, optoelectronics, biomaterials, data storage, and environmental equipment [1–5]. In the last 20 years, researchers have studied the doping effect of Cd, Cu, Mg, Mn, and Ni into zinc oxide on its optical properties [6–11]. The challenge is to determine the element(s) that need to be doped into ZnO to decrease the effect of impurities on optical properties eliminate the organic pollutants, improve the photocatalytic activity, and separate water from the pollutants. The details of these applications will be given in the following paragraphs.

Among the above-mentioned doping elements, especially Cd causes the lowest band gap value in the material; therefore, it has so many application areas in industry and environment. Mosquera et al. [12] found that the optical band gap was reduced from 3.21 eV to 3.11 eV as the CdO sample was increased. In this process, [12] observed that there were defects in CdO–ZnO nanocomposites when photoluminescence (PL) measurements were taken. They calculated the particle size from the Scherrer formula and verified it by TEM images. To study the effect of the particle size on photoluminescent intensity, Al-Hada et al. [13] used a thermal method to synthesize the binary $(ZnO)_{0.4}(CdO)_{0.6}$ nanoparticles (NPs). They found that the increased particle size calculated by the Scherrer formula led to a rise in the photoluminescent intensity. They pointed out that energy band gaps were reduced as calcination temperature was increased. By a thermal treatment technique, Al-Hada et al. fabricated binary oxide $([CdO])_x([ZnO])_{1-x}$ NPs at various doping ratios [14]. They calculated the average particle size by using the Scherrer and TEM analysis of the samples. Their TEM analysis showed that the particle sizes increased from 14 to 33 nm as concentration was increased from 20% to 80%. The X-ray photoelectron spectroscopy (XPS) analyses were used to get the surface composition of CdOZnO NPs. Using the Kubelka–Munk equation, the optical band gap was obtained with the help of diffuse UV–visible reflectance spectra. In their conclusion, Al-Hada et al. mentioned that when x concentration was increased, the energy band gap values were decreased from 3.22 to

E-mail address: ozugurlue@itu.edu.tr.

https://doi.org/10.1016/j.jallcom.2021.158620
0925-8388/

3.11 eV and 2.92–2.82 eV, for ZnO and CdO, respectively [14]. There is also antimicrobial application of cadmium doped ZnO. In 2018, Somasundaram et al. [15] reported that using the HR-TEM imaging and the Scherrer formula, when calcination temperature was increased, the mean particle size (~49 nm with the shape of a sphere) and crystallinity were also increased for CdO:ZnO nanocomposites.

In this high-tech era, there is still a problem in both daily usage of water and drinking due to the serious effects of pollution. It is known that the nanocomposite of Cadmium Oxide and Zinc Oxide (CdO ZnO) can separate the pollutants from the water. In 2019, Mahendiran et al. [16] used the Williamson–Hall (W–H) method to investigate the lattice strain and the crystallite size. In their study, they pointed out that superoxide O^{2-} radicals caused high photocatalytic activity because ZnO could efficiently trap photo-generated electrons in CdO. Liu et al. tried a different method called an auto combustion method to synthesize $Zn_{1-x}Cd_xO$ (x = 0, 0.01, 0.03, and 0.05) NPs [17]. They found that ZnCdO NPs had a hexagonal wurtzite structure with loose and porous morphologies and pointed out that Cd ions merged into ZnO crystal successfully as shown in PL and XPS spectra; as the concentration was increased from x = 0–0.03, the oxygen vacancies increased, however, it decreased at x = 0.05. Moreover, they used the Scherrer formula to calculate the crystallite grain size and found it to be 40.1, 31.8, 30.9, 32.1 nm for x = 0.00, 0.01, 0.03, and 0.05, respectively. In 2017, Santhi et al. [18] used the precipitation method to synthesize $Zn_{1-x}Cd_xO$ (x = 0.00, 0.02, 0.03, 0.04, and 0.05) NPs and found the average crystallite size as 19.6, 22.9, 23.6, 28.4, and 28.8 nm for x = 0, 0, 0.02, 0.03, 0.04, and 0.05, respectively, using the Scherrer formula. Due to the existence of polycrystalline collections, the crystallite size of the particles is not generally the same as the particle size [[19] and the references therein]. The lattice strain is affected by coherency stresses, contact or sinter stresses, the grain boundary triple junction, stacking faults. The Bragg peak position is affected by the lattice strain and crystallite size quantities and they both increase shift position and the width and intensity of the peak.

All the above-mentioned articles and most of the other works in the literature used the X-ray profile analysis which is just an average method to calculate the particle size, stress, and lattice strain, etc. To approach this problem differently, Yogamalar et al. [19] proposed the W–H analysis was more accurate to calculate the particle size, stress, and strain by considering a simplified integral breadth method where both sizes and strain-induced broadening were deconvoluted by considering the peak width as a function of 2θ.

In this study, stress, strain, and crystallite size of $Zn_{1-x}Cd_xO$ (prepared by the sol–gel method) NPs were estimated by applying various forms of Williamson–Hall procedure, such as the Uniform Deformation Model (UDM), the Uniform Stress Deformation Model (USDM), and the Uniform Deformation Energy Density Model (UDEDM) in a least-squares framework for various dopant ratios x (x = 0.01, 0.02, 0.03, 0.04, 0.05, 0.1, 0.2, and 0.3) instead of using the Scherrer formula. This estimation was also analyzed using the root mean square (*RMSE*), the coefficient of determination (R^2), the total sum of square (*SST*), the correlation coefficient, the *p*-value for F-statistic of the liner fit versus constant model. The effects of different Cd concentrations on the structural and morphological of ZnO materials were systematically studied. Moreover, in Section 4, to explore electronic and optical properties of Cd doped ZnO for x = 0.1, 0.2, and 0.3 ignoring lower concentrations due to the discursive behavior of nanocrystalline particle size concerning Cd amount in ZnO, the DFT calculations were used with GGA in the Perdew–Burke–Ernzerhof (PBE) scheme.

2. Methods

2.1. The preparation process of $Zn_{1-x}Cd_xO$ NPs

As polycrystalline form, $Zn_{1-x}Cd_xO$ (x = 0.01, 0.02, 0.03, 0.04, 0.05, 0.1, 0.2, and 0.3) NPs were synthesized using the sol–gel technique. In this process, the chemicals related to the composition of Zn acetate dehydrate and cadmium acetate tetrahydrate was used as precursor materials. The methanol and monoethanolamine were used to arrange clear homogenous solutions. At room temperature (RT), a magnetic stirrer was used to mix all the materials and they were weighed. Next, the solutions were removed from the solvent and preheated at 200–350°C for 10 min under air, for details, see [20]. Finally, for each sample, a heat treatment procedure was applied in a programmable step furnace at 600°C. The structural analysis was provided by the X-Ray diffraction measurement technique (Rigaku diffractometer) for synthesized NPs with Cu Kα radiation source. Utilizing JEOL, JSM-5910LV model Scanning Electron Microscope (SEM) tool, the microstructural properties were analyzed by using the surface morphology images.

2.2. Characterization techniques

The powder X-ray diffraction was used for the phase study of $Zn_{1-x}Cd_xO$ (x = 0.01, 0.02, 0.03, 0.04, 0.05, 0.1, 0.2, and 0.3) NPs. The Rigaku Multiflex diffractometer using Cu Kα radiation (λ = 1.5408 Å), in the scan range of 2θ between 10° and 80° with a scan speed of 3°/min and with a step increment of 0.02 was used to get the powder XRD patterns.

2.3. Statistical analysis

Using Matlab version 2018b, the linear regression model was applied to the experimental data and the MATLAB built-in function *fitlm,* which is based on the method of iterative reweighted least-squares, was used to provide the statistical analysis tools such as the root mean square (*RMSE*), the coefficient of determination (R^2), the total sum of square (*SST*), the correlation coefficient, the *p*-value for F-statistic of the liner fit versus constant model.

3. Results and discussions

3.1. Structural properties

The X-ray diffraction (XRD) of Cd-doped ZnO NPs was shown in Fig. 1. Broad peak positions and nanocrystal-line samples suggested that all samples agreed well with the standard ICDD file (ICDD Card no. 36-1451) as shown in Fig. 1. That also implied ZnO had a hexagonal structure. The (100), (002), (101), (102), (110) (103), (200), (112), and (201) planes of ZnO showed the observed peaks (in black color, in Fig. 1). The diffraction peaks indexed as (111), (200), and (220) planes of CdO showed a cubic structure (in red color, in Fig. 1). There was a single hexagonal ZnO structure up to 2% of Cd doping as shown in Fig. 1. After 2% of Cd, the secondary CdO phase appeared due to the high doping concentration. All $Zn_{1-x}Cd_xO$ (x = 0.01, 0.02, 0.03, 0.04, 0.05, 0.1, 0.2, and 0.3) NPs were obtained in the range of $10° \le 2\theta \le 80°$. The highest peak was observed on the (101) plane which signified that a preferable crystallographic (101) orientation was obtained for ZnO NPs. Tables S1 and S2 (S: the Supplementary Material) show the concentration-dependent lattice parameters, particle sizes, volume of the unit cell, the locality of the atoms and their displacement (*u*), microstrain (ε), stress (σ), dislocation density (δ) (the amount of defect in the sample), and bond length *L* using XRD analysis. The formulations of δ, d_{hkl}, *D*, *u*, *V*, and *L* parameters are given below. The following Eq. (1) was used to calculate the ZnO bond length [21]:

$$L = \sqrt{\left(\frac{a^2}{3}\right) + [0.5 - u]^2 c^2} \quad (1)$$

where *a* and *c* are the lattice constants of ZnO, as shown in Fig. S1 (see the Supplementary Material), and *u* is the wurtzite structure and its calculation is given in Eq. (2) as:

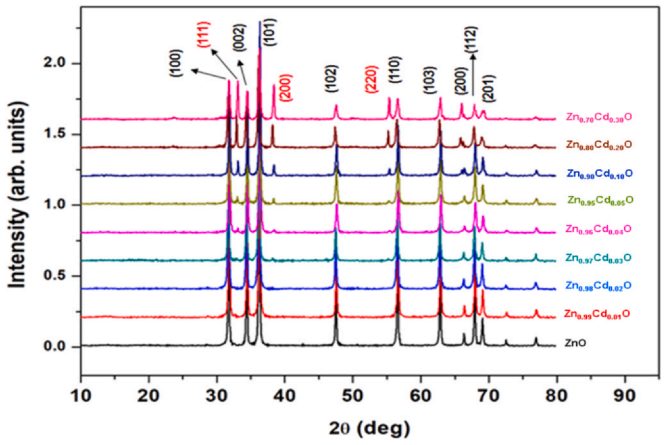

Fig. 1. The powder XRD patterns of all $Zn_{1-x}Cd_xO$ (x = 0.01, 0.02, 0.03, 0.04, 0.05, 0.1, 0.2, and 0.3) NPs prepared by the sol–gel method. ZnO and CdO planes were shown in black color and red color, respectively (For interpretation of the references to color in this figure legend, the reader is referred to the web version of this article).

$$u = \left(\frac{a^2}{3c^2}\right) + 0.25 \tag{2}$$

Using the XRD pattern, the following formula was used for calculation of the lattice constants a and c [21] where d is the spacing between planes of given the Miller indices h, k, and l:

$$\frac{1}{d_{hkl}^2} = \frac{4}{3}\left(\frac{h^2 + hk + k^2}{a^2}\right) + \frac{l^2}{c^2} \tag{3}$$

The average particle sizes were calculated by using the highest three XRD peaks (100), (002), and (101) based on the Scherrer formula as shown in Eq. (4) [21]:

$$D = \frac{K\lambda}{\beta_{hkl}\cos(\theta)} \tag{4}$$

where β_{hkl} is the integral half-width, $K = 0.9$, λ is the wavelength of the incident X-ray ($\lambda = 0.1540$ nm), D is the average particle size, and θ is the Bragg angle. The following equation was used to calculate the unit cell volume (V), as shown in Eq. (5):

$$V = 0.866 \quad a^2c \tag{5}$$

The physical defects and dislocation densities (δ) may increase due to stress and strain in the crystal structures. Thus, the dislocation density was calculated using Eq. (6) taking into account the amount of defect in the sample, as shown in Table S2.

$$\delta = \frac{1}{D^2} \tag{6}$$

Having a low δ is crucial for a good and fine crystallinity, as exhibited in Table S2.

An inverse behavior between Zn-O bond lengths (L) and c/a values was detected, as depicted in Tables S1 and S2, as displayed in Fig. S2. Bond length values make a zigzag behavior up to x = 0.2 and a minimum at x = 0.04. However, all calculated bond lengths are in the range of 1.97082–1.98096 Å which causes a decrease in the electromechanical responses. Moreover, the value of c/a is minimum for 30% Cd concentration, as shown in Table S1. The lattice stability may be the reason why $\frac{c}{a}$ ratios are in the range of 1.599–1.603 away from the ideal value of 1.633, which might indicate the presence of oxygen vacancies and/or zinc vacancies. For the $Zn_{0.97}Cd_{0.03}O$ sample, the maximum values were obtained for L, c/a, and V. When Cd concentrations in the samples are increased, there is almost an unstable behavior called oscillation in δ and u, as shown in Table S2 and Fig. S3. The u value gradually increases for $0.01 \leq x \leq 0.04$ and $0.1 \leq x \leq 0.3$ as Cd doping increases showing an enhancement of lattice distortion with Cd-doping due to the size difference between Cd^{2+} (0.97 Å) and Zn^{2+} ions (0.74 Å). Adding a small amount of cadmium distorts the crystallographic alignment of the unit cell of the ZnO crystal and causes a high loss in the symmetry of the unit cell which may also be attributed to the difference in the ionic radii, where the ionic radius of Cd^{2+} (0.97 Å) is greater than the ionic radius of Zn^{2+} ions (0.74 Å).

To check whether the system is distorted or not, the degree of distortion is calculated using Eq. (7):

$$R = \frac{(2a\sqrt{2/3})}{c} \tag{7}$$

where R is the degree of distortion; a and c are the lattice parameters given in Table S1. The values of R are in the range 1.017 – 1.021 meaning that our system has just a little distortion, as shown in Table S1 and Fig. S4. Table S1 shows the atomic packing factor ratio c/a and the degree of distortion for varying Cd concentrations. Since a and c are the lattice parameters given in Table S1, the atomic packing fraction (APF) can also be expressed and calculated using Eq. (8):

$$APF = \frac{2\pi a}{3\sqrt{3}\,c} \tag{8}$$

The calculated values of APF and the volumes of the unit cells (V) are displayed in Table S1 and shown in Fig. S5 for varying Cd concentrations, it is obvious that the APF values are around a concentration of Cd content of about 76%, note that the APF is inversely proportional to the concentration of Cd content.

The average particle sizes, atomic packing factors (c/a), lattice parameters, the volume of the unit cells (V), degree of distortions (R), and atomic packing fractions (APF) of $Zn_{1-x}Cd_xO$ (x = 0.01, 0.02, 0.03, 0.04, 0.05, 0.1, 0.2, and 0.3) NPs were given in Table S1. Table S2 shows that concentration-dependent dislocation density δ and displacement u values become maximum for the $Zn_{0.7}Cd_{0.3}O$ sample. Also, the bond lengths are minimum at 4% Cd concentration.

3.2. Williamson–Hall (W–H) analysis

To get information on the crystallite size D, the Scherrer formula can be enough but that formula does not provide information on the strain effect in the crystal. Furthermore, it is a fact that there is a contribution to the line broadening by ε and D. Stokes and Wilson [21] observed

$$\varepsilon = \frac{\beta_{hkl}}{4 \quad \tan(\theta)} \tag{9}$$

as the average strain and the broadening arose from a small crystallite size. The Eqs. (4) and (9) tell us that both ε and D depend on θ differently. The W-H analysis method separates these two effects. Note that the integral half-width β_{hkl} (i.e. broadening) is proportional to tan (θ) due to ε. Using the W–H, the lattice strain ε, stress σ, energy density u and particle size D were estimated by applying various forms of Williamson–Hall procedure, such as the Uniform Deformation Model (UDM) to calculate ε and D, the Uniform Stress Deformation Model (USDM) to calculate ε, σ, and D, and the Uniform Deformation Energy Density Model (UDEDM) to calculate ε, σ, u, and D.

3.2.1. The uniform deformation model (UDM)

To separate the size and strain broadening present in XRD peaks is a difficult task. Williamson–Hall proposed a mathematical formula involving the crystallite size and the strain broadening to separate these two effects. Mote et al. [22] improved this expression and obtained Eq. (10):

$$\beta_{hkl}\cos(\theta_{hkl}) = \frac{K\lambda}{D} + 4\,\varepsilon sin\,(\theta_{hkl}) \tag{10}$$

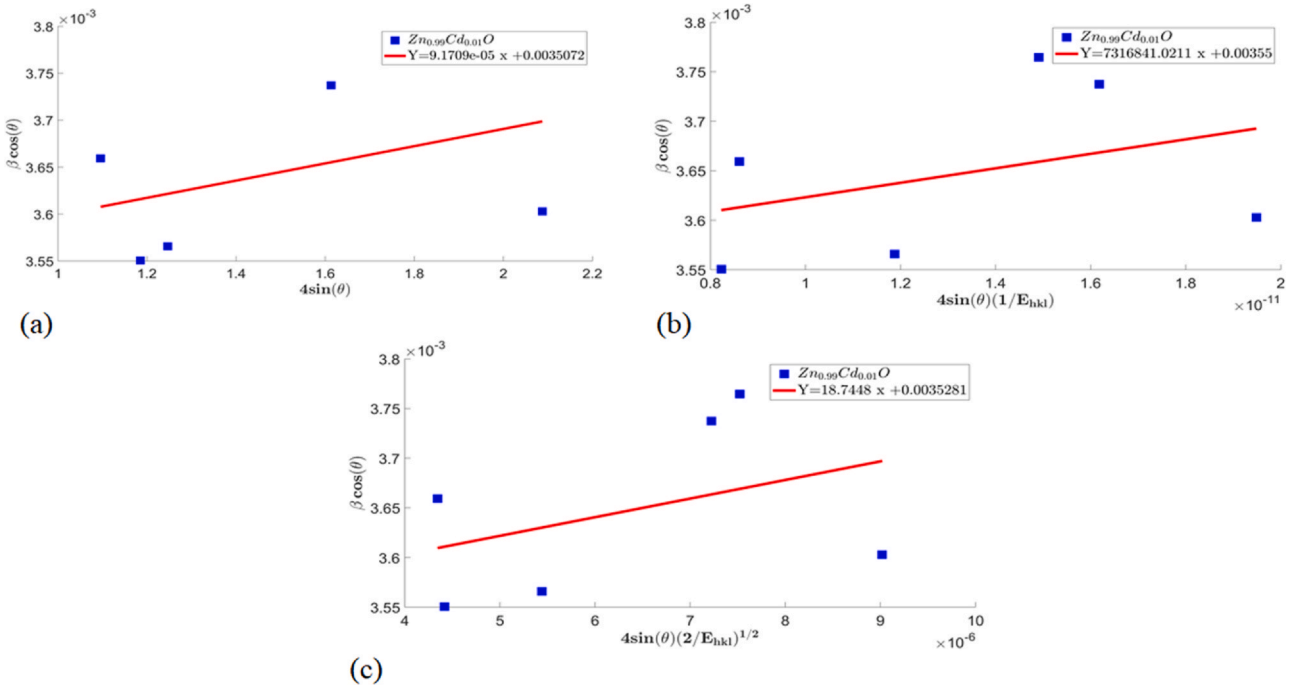

Fig. 2. $Zn_{0.99}Cd_{0.01}O$: The plots of (a) of $\beta\cos(\theta)$ vs. $4sin(\theta)$, (b) $\beta\cos(\theta)$ vs. $sin(\theta)(1/E_{hkl})$, and (c) $\beta\cos(\theta)$ vs. $4sin(\theta)\sqrt{2/E_{hkl}}$.

Fig. 2(a) exhibits the x-axis as $4\epsilon sin(\theta_{hkl})$ and the y-axis as $\beta_{hkl}\cos(\theta_{hkl})$ which is described as the UDM for $Zn_{0.99}Cd_{0.01}O$ and other cases are given in Figs. S6 and S7. The linear least-squares fitting, $y(t) = A \times t + B$, was applied to determine approximately the slope of the graph of $\beta\cos(\theta)$ where A and B were found by minimizing the following error formula:

$$E(A, B) = \sum_{i=1}^{N} [(B + At_i) - Y_i]^2 \tag{11}$$

Note that ϵ is the slope of this linear fit and the crystallite size D can be found once the y-interception of $\beta\cos(\theta)$ is known, i.e. $D = \frac{K\lambda}{y_{interception}}$. Table S3 gives the crystallite size and lattice strain based on the UDM for Cd-doped ZnO NPs. It is clear that the crystallite size has a maximum value of 49.36 nm for 5% Cd and the corresponding slope of the fit is also maximum insinuating that the lattice strain has a maximum value of 7×10^{-4}, as shown in Table S3. It is also observed that crystallite size decreases, and strain increases up to 2% Cd doping, after that, both crystallite size and strain started to oscillate with increasing Cd doping, and this is an indication of the secondary phase of CdO. Table S4 presents the optimized A and B values, here $N = 6$ (the number of the first six reflection peaks), and the relative errors for each Cd concentration. The plot of $\beta\cos(\theta)$ versus $4sin(\theta)$is given in Fig. 2(a) where the linear fit is plotted in a red line. All the linear fits have a positive slope except for the $Zn_{0.96}Cd_{0.04}O$ sample, as shown in Table S4. We present the statistics in Table S4 and discuss them in Section 3.3.

3.2.2. The uniform stress deformation model (USDM)

The UDM assumes that uniform strain is present in all crystallographic directions. However, this is not true for NPs, the anisotropic nature of the Young modulus of the crystal must be taken into consideration which is more realistic, thus uniform stress deformation model and uniform energy density deformation model are introduced just to achieve this task [22].

Mote et al. [22] derived the following equation by considering σ/E_{hkl} in the UDM instead of the isotropic lattice strain ϵ_{hkl}, this new model is named the USDM, where E_{hkl} is the Young modulus in the direction$\perp$ to the set of planes < hkl >. Hence, Eq. (10) becomes

$$\beta_{hkl}\cos(\theta_{hkl}) = \frac{K\lambda}{D} + \quad 4 \quad \sigma/E_{hkl}sin(\theta_{hkl}) \tag{12}$$

The Young's modulus E_{hkl} [24,25] is given by

$$E_{hkl} = \frac{\left[h^2 + \frac{(h+2\ \ k)^2}{3} + \left(\frac{a}{c}\right)\right]^2}{S_{11}\left[h^2 + \frac{(h+2\ \ k)^2}{3}\right]^2 + \quad S_{33}\left(\frac{al}{c}\right)^4 + (2 \quad S_{13} + S_{44})\left[h^2 + \frac{(h+2\ \ k)^2}{3}\right]\left(\frac{al}{c}\right)^2} \tag{13}$$

which is related to their elastic compliances $S_{ij}[m^2N^{-1}]$ where $S_{11} = 7.858 \times 10^{-12}$, $S_{13} = -2.206 \times 10^{-12}$, $S_{33} = 6.94 \times 10^{-12}$, $S_{44} = 23.57 \times 10^{-12}m^2N^{-1}$ having a hexagonal crystal phase. Eq. (12) represents the USDM in which the strain is assumed to be used uniform in all crystallographic directions. When the graph is plotted between $\beta\cos(\theta)$ and $4sin(\theta)(1/E_{hkl})$, then the lattice strain ϵ_{hkl} can be evaluated as σ/E_{hkl} where the slope of the linear fit is the uniform stress σ and the interception on the $\beta\cos(\theta)$ axis gives crystallite size D, i.e. $D = \frac{K\lambda}{y_{interception}}$. The plot of $\beta\cos(\theta)$ versus $4sin(\theta)(1/E_{hkl})$ (the USDM) for $Zn_{0.99}Cd_{0.01}O$ is shown in Fig. 2(b) and other cases are given in Figs. S8 and S9. Table S3 presents the stress, lattice strain, and crystallite size estimated by the USDM. The stress calculated from the slope of the line has a maximum value of 60.4×10^6 for 5% Cd doping. The secondary phase of CdO which appears after 2% Cd doping is primarily the reason for the observed oscillations in crystallite size, stress, and strain in the Cd-doped ZnO NPs. The maximum crystallite size is 44.69 nm for 5% Cd doping according to the USDM. Linear least-squares fitting, $y(t) = A \times t + B$, is applied to determine approximately the slope of the graph of $\beta\cos(\theta)$, the error function was given in Section 3.2.1 with Eq. (11). Table S4 presents the optimized A and B values, here $N = 6$ (the number of the first six reflection peaks), and the relative errors for each Cd concentration.

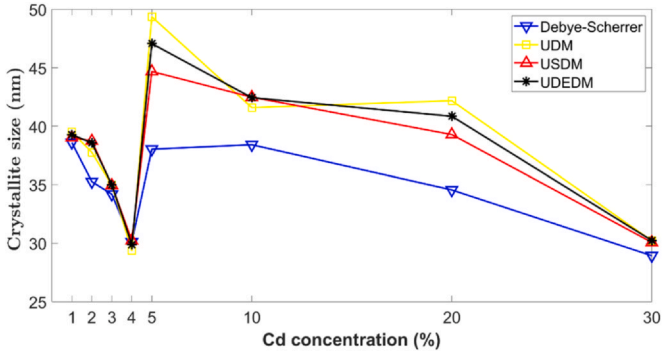

Fig. 3. The crystallite size (D) values for all different methods, namely, the Scherrer, the UDM, USDM, and UDEDM vs. Cd concentration (%) for $Zn_{1-x}Cd_xO$ structures (x = 0.01, 0.02, 0.03, 0.04, 0.05, 0.1, 0.2, and 0.3).

3.2.3. *The uniform energy density deformation model (UDEDM)*

To calculate the energy density (u) of a crystal, Mote et al. [22] also introduced another model of Williamson–Hall analysis named the UDEDM. In this method, a deformation energy density is assumed to be the cause of anisotropic strain. Since the UDEDM is uniform, then strain ε and the energy density u are related, as shown in Eq. (14):

$$u_{ed} = \frac{\varepsilon^2 E_{hkl}}{2} \tag{14}$$

based on Hook's law. Thus, Mote et al. [22] modified Eq. (12) to obtain Eq. (15):

$$\beta_{hkl}\cos(\theta_{hkl}) = \frac{K\lambda}{D} + 4\,(2\,u_{ed}/E_{hkl})^{\frac{1}{2}} sin\,(\theta_{hkl}) \tag{15}$$

Eq. (15) represents UDEDM. If $\beta_{hkl}\cos(\theta_{hkl})$ and $4(2/E_{hkl})^{\frac{1}{2}} sin\,(\theta_{hkl})$ are considered as the y-axis and the x-axis, respectively, then by using a linear least-squares method the slope of the linear fit gives approximately the energy density u and the interception on the $\beta\cos(\theta)$-axis gives the crystallite size D, i.e. $D = \frac{K\lambda}{y_{interception}}$. Fig. 2(c) depicts the plot of $\beta\cos(\theta)$ versus $4sin(\theta)\sqrt{2/E_{hkl}}$ (the UDEDM) for $Zn_{0.99}Cd_{0.01}O$ and other cases are given in Figs. S10 and S11. Table S3 presents the stress, crystallite size, lattice strain, and energy density estimated by the UDEDM. As the Cd concentration increases, an oscillation behavior in the energy density$u$ materializes. According to the UDEDM, a maximum value of 47.07 nm for 5% Cd occurs for the crystallite size.

The linear least-squares fitting, $y(t) = A \times t + B$, was applied to determine approximately the slope of the graph of $\beta\cos(\theta)$, the error function was given in Section 3.2.1 with Eq. (11). Table S4 presents the optimized A and B values, here $N = 6$ (the number of the first six reflection peaks), and the relative errors for each Cd concentration.

Among all the W–H models mentioned above, the results obtained by the USDM are consistent with the reported literature [16]. From Table S3, the crystallite sizes of all samples determined by the USDM match with TEM results except for $x \geq 0.05$ Cd concentrations [16]. Using the UDEDM, the average and maximum stress and

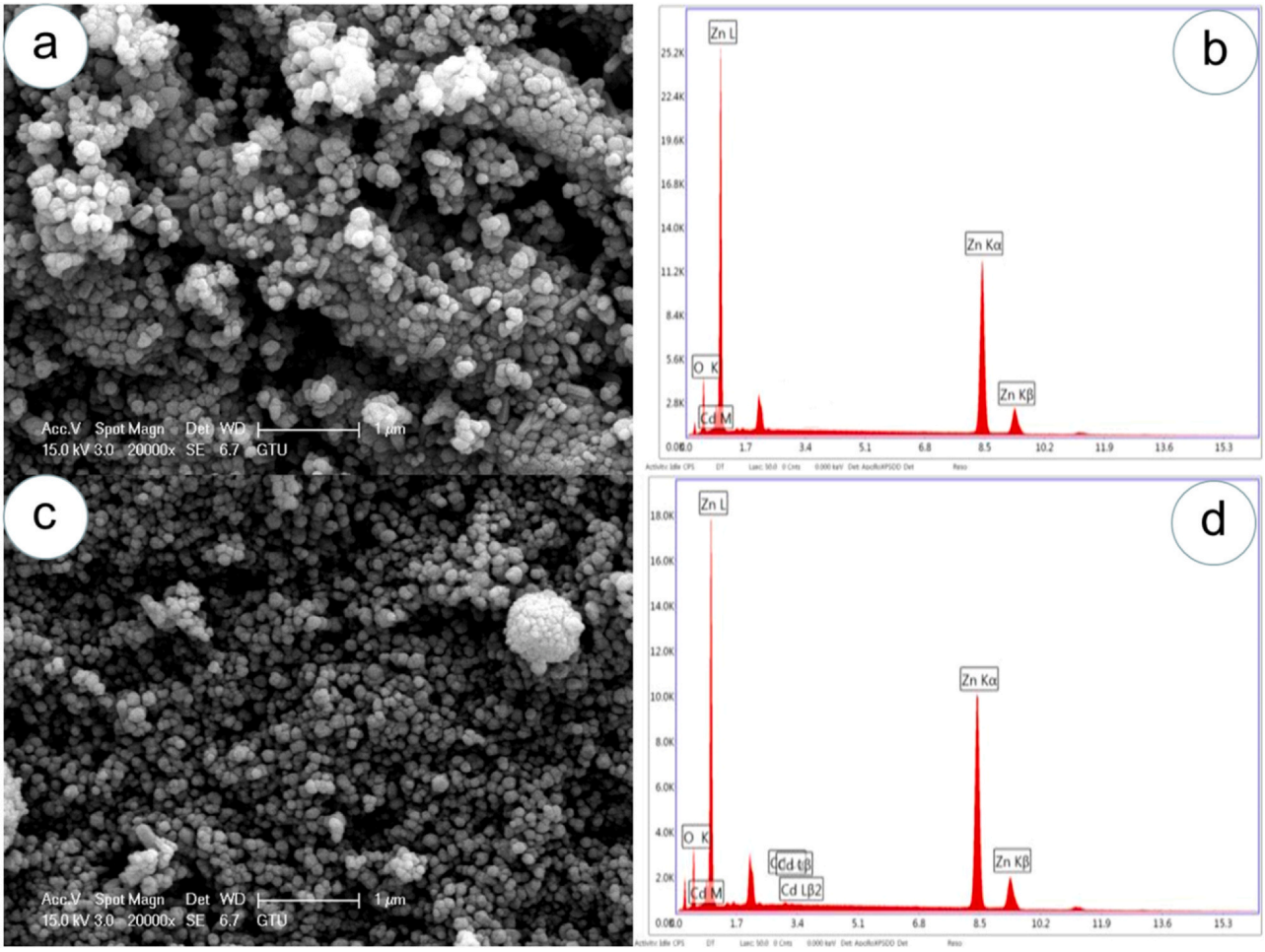

Fig. 4. SEM images of ZnO and $Zn_{0.99}Cd_{0.01}O$ compositions for 1 μm magnifications in (a) and (c) respectively, the EDX graphs of ZnO and $Zn_{0.99}Cd_{0.01}O$ sample in (b) and (d).

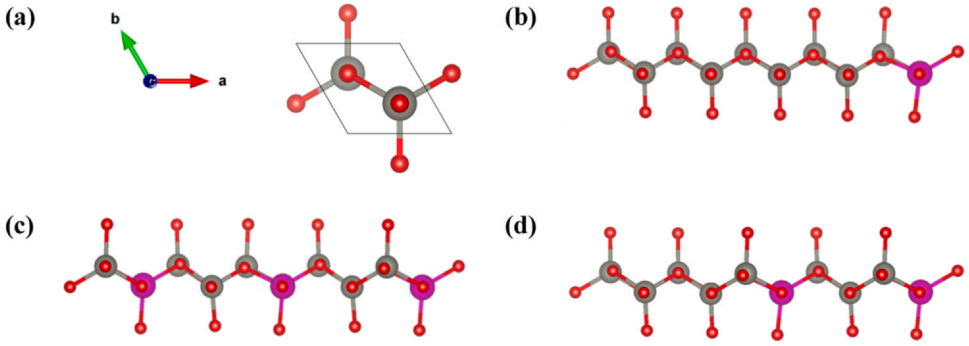

Fig. 5. (a) Unit cell and supercell of (b) 10%, (c) 20%, and (d) 30% of Cd where purple, red, and gray spheres represent cadmium, oxygen, and zinc, respectively (For interpretation of the references to color in this figure legend, the reader is referred to the web version of this article).

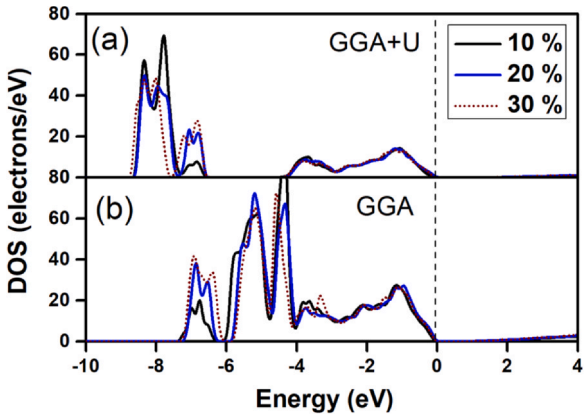

Fig. 6. TDOS of ZnCdO for 10, 20 and, 30% of Cd (a) including Hubbard term (b) without Hubbard term.

microstrain values are obtained from the first six peak planes, as shown in Fig. 1 and reported in Table S3. Contrary to the results of Mote et al., it is observed that the USDM is more suitable for NPs than the UDEDM. Table S1 shows the results obtained from the Scherrer formula and Table S3 for the UDM, USDM, UDEDM. The average microstrain values of the NPs obtained from the USDM are more similar which means energy density and stress are affected by the average microstrain. Our results agree with the findings of Mahendiran et al. [16]. The ICDD data file (ICDD Card no. 36-1451) of ZnO confirms the data obtained from the X-ray diffraction for the planes (103), (110), (102), (101), (002), and (100) with their lattice parameters and diffraction peaks. Table S5(a–h) displays the calculated strain and stress values for these planes.

In Table S4, the linear fits have a positive slope, i.e. the uniform stress (σ) and indirectly lattice strain ε are positive except for the $Zn_{0.96}Cd_{0.04}O$ sample. Tables S3 and S5(a–h) show that the σ values are less than zero indicating compressive stress. Since the stress values in most of the samples are positive, it can be concluded that the structures undergo tensile stress. The positive slope value shows the tensile strain. This also indicates anisotropic microstrain due to the presence of point defects. In Fig. 3, concentration-dependent crystallite size (D) values calculated with four different methods, namely, the Scherrer, the UDM, USDM, and UDEDM for $Zn_{1-x}Cd_xO$ (x = 0.01, 0.02, 0.03, 0.04, 0.05, 0.1, 0.2, and 0.3)NPs are plotted. Note that the crystallite sizes fluctuate as the concentration increases up to 5%, afterward crystallite size decreases as the concentration increases. We present the statistics in Tables S6–S8 for the UDM, USDM, and UDEDM, respectively and discuss in Section 3.3.

3.3. Statistical analysis

We used the built-in *fitlm* function of MATLAB to measure the accuracy of our linear regression model and provided the necessary statistics to show how well the model estimates match with the observed responses. We present these statistics in Tables S6–S8 for the UDM, USDM, and UDEDM, respectively. Even though the RMSE and SST values are around 10^{-4} and 10^{-7}, respectively, these are not enough by themselves to confirm that our linear regression models provided good fits. From these tables, one can conclude that the linear model for the $Zn_{0.95}Cd_{0.05}O$ sample provides a good fit since the coefficient of determination (R^2) is closer to 1 than the other samples. For 5% Cd concentration, the correlation coefficients are above 0.9 indicating the strongest possible agreement. However, looking only at the R^2 values and the correlation coefficient might be misleading since one has to consider the F-statistic that compares our linear regression model against the constant model. The p-value

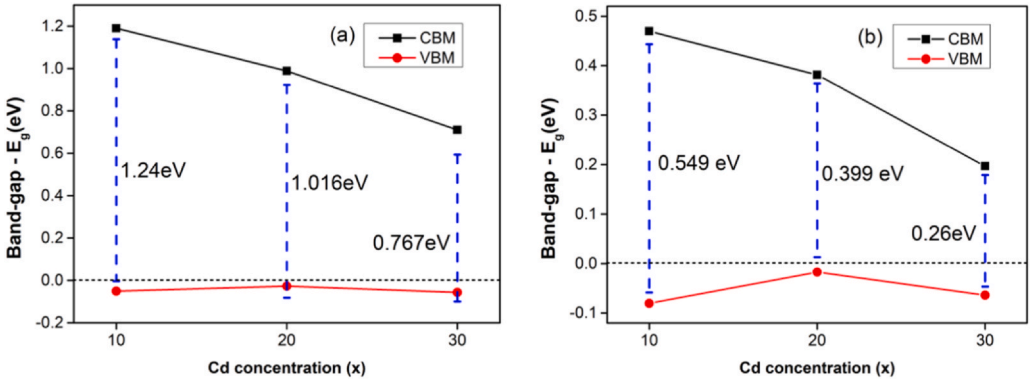

Fig. 7. Bandgaps for 10, 20 and, 30% of Cd (a) with Hubbard term (b) without Hubbard term.

of the model is an indicator of the F-statistic. One can see that the best results are for 5% Cd concentration, where the *p*-values were 0.0018, 0.0202, and 0.0061 for the UDM, USDM, and UDEDM, respectively. In other cases, either our model provides a poor fit for our data, or the number of data is not enough.

3.4. The morphology characteristics of $Zn_{1-x}Cd_xO$ NPs

The SEM technique was used in the range 1 µm magnifications for the morphology of all $Zn_{1-x}Cd_xO$(x = 0.01, 0.02, 0.03, 0.04, 0.05, 0.1, 0.2, and 0.3) NPs.

For example, without any specific reason, the SEM images of ZnO and $Zn_{0.99}Cd_{0.01}O$ compositions for 1 µm magnifications were only chosen to be plotted because of the space limitations. As seen in Fig. 4(a) and (c), there is a random particle distribution and the distribution of particles is prevailed by particle gathering. Fig. 4(b)–(d) exhibited the EDX plots showing the chart and elemental compounds of ZnO and $Zn_{0.99}Cd_{0.01}O$. For x = 0.00, only Zn and O ions were observed in the EDX spectra as displayed in Fig. 4(a). In Fig. 4(b) at x = 0.01, the EDXA spectra confirm all the ions of the sample in ZnCdO. The EDX plots also confirm the correct ratios of atomic percentages. The crystallite size obtained by Debye-Scherrer is inversely proportional to maximum microstrain and stress values obtained by W–H models, as illustrated in Figs. S12 and S13, respectively. Fig. S14 displays SEM images of $Zn_{0.98}Cd_{0.02}O$ and $Zn_{0.97}Cd_{0.03}O$ compositions for 1 µm magnifications in (a) and (c) respectively, the EDX graphs of $Zn_{0.98}Cd_{0.02}O$ and $Zn_{0.97}Cd_{0.03}O$ samples in (b) and (d). Fig. S15 gives SEM images of $Zn_{0.96}Cd_{0.04}O$ and $Zn_{0.95}Cd_{0.05}O$ compositions for 1 µm magnifications in (a) and (c) respectively, the EDX graph of $Zn_{0.96}Cd_{0.04}O$ and $Zn_{0.95}Cd_{0.05}O$ samples in (b) and (d). Finally, Fig. S16 shows SEM images of $Zn_{0.9}Cd_{0.1}O$, $Zn_{0.8}Cd_{0.2}O$, and $Zn_{0.7}Cd_{0.3}O$ compositions for 1 µm magnifications in (a), (c), and (e) respectively, the EDX graphs of $Zn_{0.9}Cd_{0.1}O$, $Zn_{0.8}Cd_{0.2}O$, and $Zn_{0.7}Cd_{0.3}O$ samples in (b), (d) and (f). This tells us that the Cd^{2+} ions were appropriately replaced into the ZnO lattice.

The peaks of all intended compositions are obtained in EDX analysis, this is an indication of well-prepared samples.

3.5. Electrical and optical properties: first-principles calculations

To examine electronic and optical properties of Cd-doped ZnO for x = 0.1, 0.2, and 0.3 ignoring lower concentrations due to the discursive behavior of nanocrystalline particle size respect to Cd amount in ZnO, we used CASTEP [23] to do DFT calculations with GGA in the PBE scheme. According to the short period findings, GGA-PBE is suitable for the rest calculations due to the consumed time and pretty sensitive results when compared with firstly HSE/PBE0 and then rest. Hence, the GGA-PBE was used during calculations of electronic and optical properties while energy minimization. Moreover, the GGA of PBE [24] was picked since it describes the chemical bond energies. An ultrasoft pseudopotential was used to present the electron-ion interactions with Koelling–Harmon relativistic treatment and the energy cut-off was set to 450 eV. Electronic configurations of corresponding atoms Zn, Cd and O, in short valance configurations were treated as 3s2 3d10 4s2, 4d10 5s2 and 2s2 2p4, respectively. We considered Hubbard correction to provide a reasonable consistency to experimental findings via setting U_{Zn}

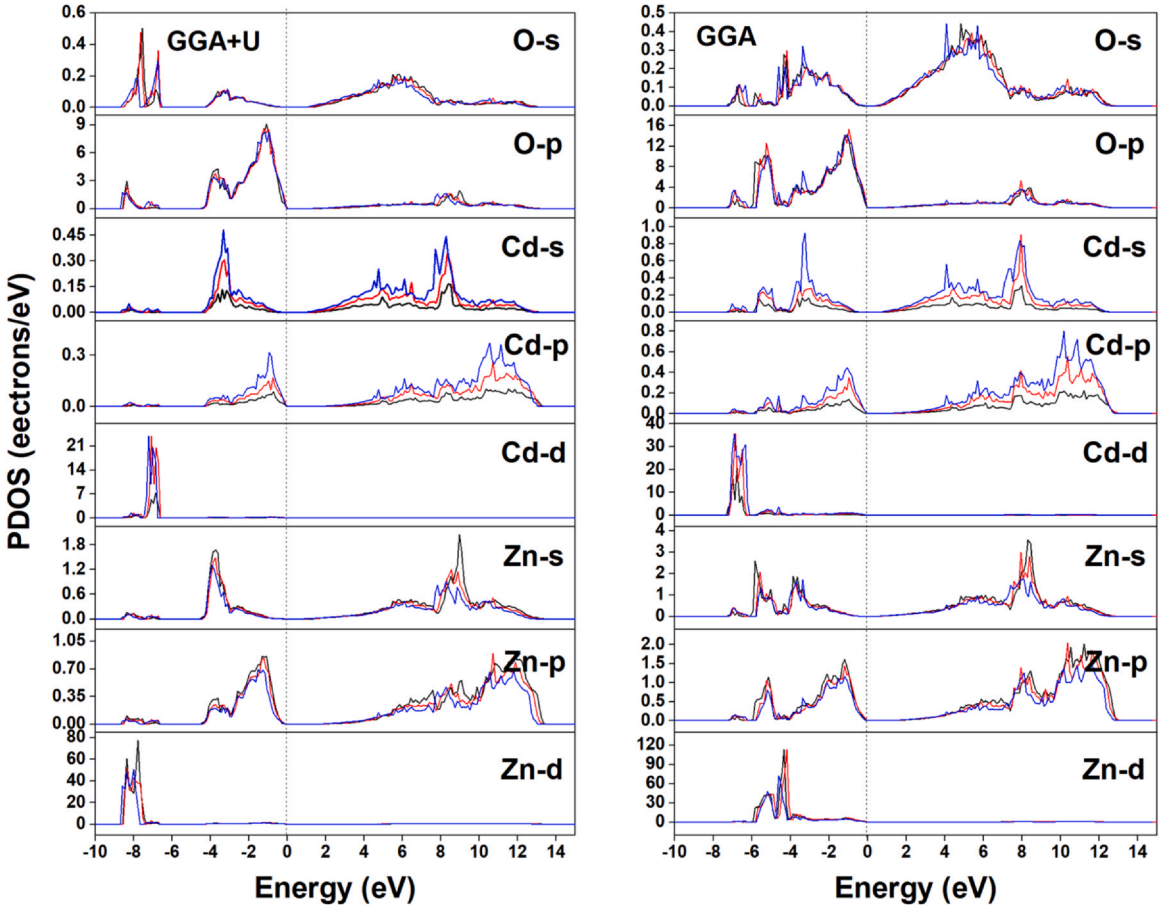

Fig. 8. PDOS of Cd (a) including Hubbard term (b) without Hubbard term. Black, red, and blue lines represent 10%, 20%, and 30% Cd concentration, respectively (For interpretation of the references to color in this figure legend, the reader is referred to the web version of this article).

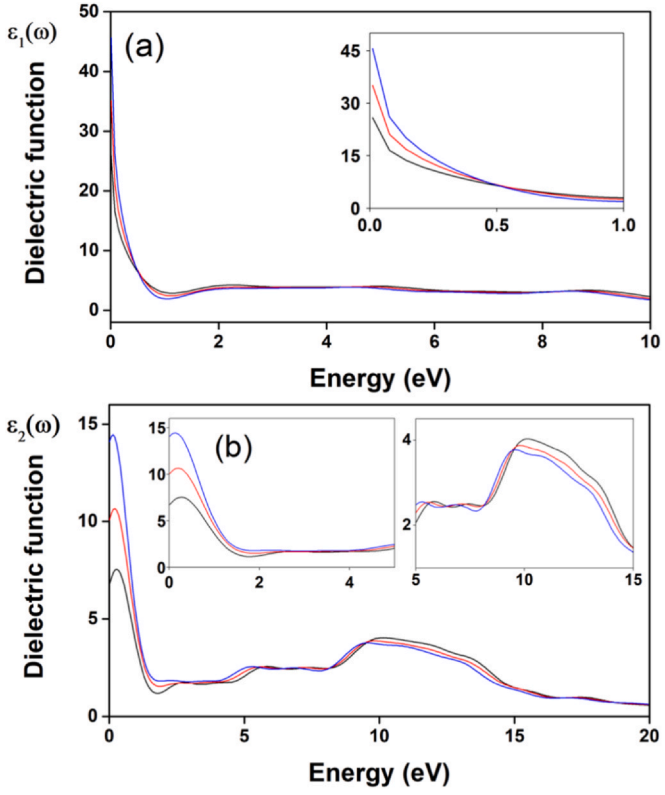

Fig. 9. (a) The real part ε_1 (ω) and (b) the imaginary part ε_2 (ω) of the dielectric function. Black, red, and blue colors represent 10%, 20%, and 30% Cd concentration. Insets were used to focus on certain photon energy intervals (For interpretation of the references to color in this figure legend, the reader is referred to the web version of this article).

= 9 eV, U_{Cd} = 2 eV and U_O = 5 eV [25,26]. To satisfy a volume uniform distribution of Cd in supercell structure [27], a 5 × 1 × 1 packed supercell was constructed via implementing the lattice parameters, a (Å) and c (Å) as illustrated in Table S1. To achieve the desired doping concentration of Cd/Zn, Cd ions were interchanged with host Zn sites, in the meantime, corresponding a (Å) and c (Å) values were updated. SCF and band energy tolerance values were set to 1e-7 eV/cell and 1e-7 eV, respectively. A 20 atoms (10 Zn and 10 O) wurtzite hexagonal supercell was prepared as given in Fig. 5. Electronic properties were enlightened through the total and partial density of states (DOS) and theoretical bandgap; herewith, the dielectric constant matrix was calculated to reveal optical properties examining adsorption and reflectivity in the light of refractive index.

Firstly, to focus on electronic properties related to Cd concentration (x), the density of states was handled in the atomic and orbital scheme through elucidating VB and CB energy contributions including the Fermi level. All dopant concentrations (10, 20 and, 30% of Cd) contributed to electronic energies between −4 eV and Fermi level at VB almost equally for both cases (GGA and GGA+U) (Fig. 6). Hubbard interaction caused to vanish the electronic states below −4 eV up to −6.5 eV until they reappeared at deeper parts of VB with maximum contribution as shown in Fig. 6(a). On the other hand, electronic states occurred continuously at VB in the absence of Hubbard term even a sudden death occurred at ~−6 eV. Although a change in Cd concentration did not dramatically affect the electronic state at calculated energies, there is an increment in state density when the amount of guest material is increased between −6 eV and −7 eV in both cases (GGA and GGA+U). One can note that GGA+U provides a higher bandgap.

According to Fig. 7, the conduction band maximum (CBM) is lowered by increasing Cd concentration even if the valance band minimum (VBM) did not show any stabile tendency directly related to the amount of guest material. The calculated band gap energy by GGA+U is almost 2.5 times of bandgaps of GGA which is also higher than [28] findings. Note that VBM seems to be always closer to Fermi level and direct bandgap is observed in interested Cd concentration. Thus, one can deduce that the high bandgap tuned via CBM instead of VB states.

To elaborate on the orbital contributions to the electronic state of interesting material, the partial density of states (PDOS) were studied. The increasing amount of guest atom within ZnO contributed to the electronic structure at both VB and CB energies as shown in Fig. 8.

Crystallite size showed a decrement trend for Cd amount of > 10% despite a random behavior that emerged for lower concentrations (Fig. 3). One can conclude that bandgap is decreased when crystallite size is reduced through increasing guest concentration.

Hubbard term provides an increment on the number of disallowed states around the Fermi level widening the band gap (Fig. 8). Although d-orbitals were not dramatically affected by the U term, there is a shift at deeper regions of Zn-d VB. Cd and O possess a worthy contribution to the widened bandgap. However, in GGA only calculation, between −6 eV and −4 eV, there is an additional electronic state density presence that affected the VB. DOS weakened when the U term is included in the calculation in contrast to the increment trend in the bandgap. Electronic state density of Cd-s, Cd-p, and Cd-d orbitals was improved through increasing Cd amount in ZnO for both cases (GGA and GGA+U) (Fig. 8) despite an inversely proportional relation between Zn orbitals DOS and Cd concentration. Optical properties were studied by firstly calculating the transverse dielectric function $\varepsilon(\omega) = \varepsilon_1(\omega) + i\varepsilon_2(\omega)$. There are two transitions associated with ε (ω) known as intraband and interband transitions. ε_1 (ω) was obtained from the Kramers–Kronig relation and given by Eq. (16):

$$\varepsilon_1(\omega) = 1 + \frac{2}{\pi} p \int_0^{\infty} \frac{\varepsilon_2(\omega')\omega' \varepsilon_2 d\omega'}{\omega'^2 - \omega^2} \tag{16}$$

where the principal value of the integral is p [29,30] and ε_1 (ω) is the amount that the light is stopped by a material. The following equation was used to calculate ε_2 (ω) which demonstrates the energy absorbed from an electric field:

$$\varepsilon_2(\omega') = \left(\frac{h^2 e^2}{\pi m^2 \omega^2}\right) \sum_{C,V} \int d^3k \langle V_k | p^a | C_k \rangle \langle V_k | p^b | C_k \rangle x \delta\left(\varepsilon_{C_k} - \varepsilon_{V_k} - \omega\right) \tag{17}$$

where C_k is the valence band, V_k is the conduction band, k is the crystal momentum, p represents the moment matrix component between the bands a and b. The complex dielectric constant is an important intrinsic property. The imaginary part of the dielectric function had the majority from 0 to 2 eV; that is to say, the low-frequency region had the key importance in contrast to the rest. Besides, it was lowered by the decreasing amount of Cd. A secondary major peak was observed almost at 10 eV which corresponds to an extreme UV region with 124 nm wavelength for 10% Cd. Higher amounts possessed a slight relative redshift (Fig. 9b). However, the major peak of the real part was almost 3 times of ε_2 (ω) corresponding to very low photon energy close to zero. Real part values decreased by increasing energy. Secondly, at a certain energy, the real part took lower values when the Cd amount is fewer. Latter is valid up to 0.5 eV; immediately after the scenery was changed as the opposite up to 3 eV.

The energy loss function *L(w)* of ZnCdO measures the energy loss by fast-moving electrons while navigating in Cd doped ZnO NPs. The major peak in *L(ω)* is located at ~33 eV while a secondary peak emerged around ~19 eV with lowering loss via increasing Cd concentration. Due to the presence of Cd atoms, this peak is located at higher energy compared to [31,32] for non-doped ZnO. The major peak in the WZ phase is located at 23.30 eV and is blue-shifted

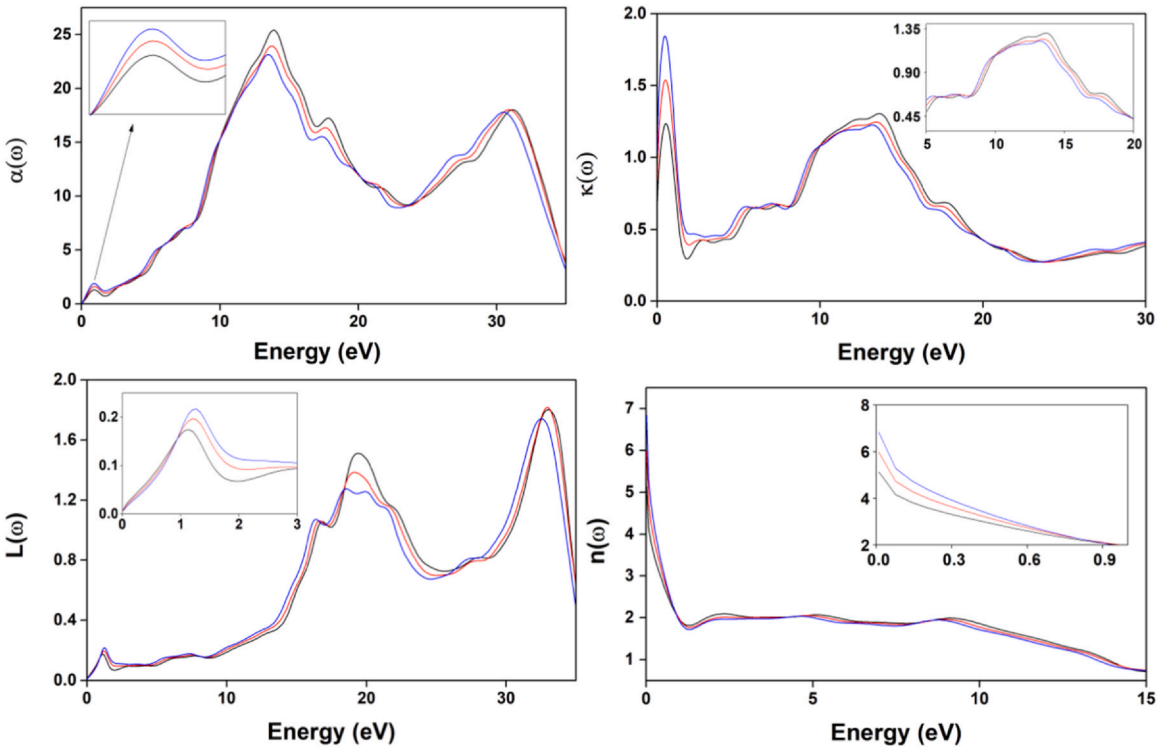

Fig. 10. α, κ, L, and n represent absorption coefficient, extinction coefficient, energy loss function, and refractive index related to photon energy while black, red, and blue lines correspond to 10%, 20%, and 30% of Cd concentration, respectively (For interpretation of the references to color in this figure legend, the reader is referred to the web version of this article).

compared to the ZB phase similar to the findings of Zhang et al. [28], as depicted in Fig. 10. The refractive index (n) showed behavioral similarity to the real part of dielectric function even n(w) values were quite low.

Almost 2 main peaks were observed at the absorption coefficient vs. energy relation. The absorption was enhanced at ~12.5 eV and 31 eV, respectively, and which correspond to the UV region. A redshift emerged at a secondary peak for 30% Cd. In the case of low frequencies relatively weak peak at ~1240 nm along the near-infrared region (NIR) was observed and, in contrast to the behavior at the majestic peak, Cd led an enhancement on absorption through an increasing trend (Fig. 10).

A redshift was observed according to the absorption spectra of the visible region which is more obvious by increasing Cd amount. Bai et al. reported the absorbance of 3–7% Cd at the UV region is strong at 370 nm wavelength [33]. We found a sharp peak at ~1 eV which corresponds to the IR region. For proper usage of ZnCdO in optoelectronic devices meticulously, the reflectivity $R(w)$ was investigated which is shown in the inset of Fig. 11. Reflectivity had two main peaks in which major one belongs to the far-infrared region (FIR) possessing a high frequency and, the latter is at the extreme UV side at ~14 eV photon energy. That can be occurred due to inter-band transitions. Also, at certain energies reflectivity was lowered by decreasing the concentration of Cd in ZnO at the FIR side in contrast to the latter one. Note that there is a literal non-linearity in both optical quantities as a function of photon energy.

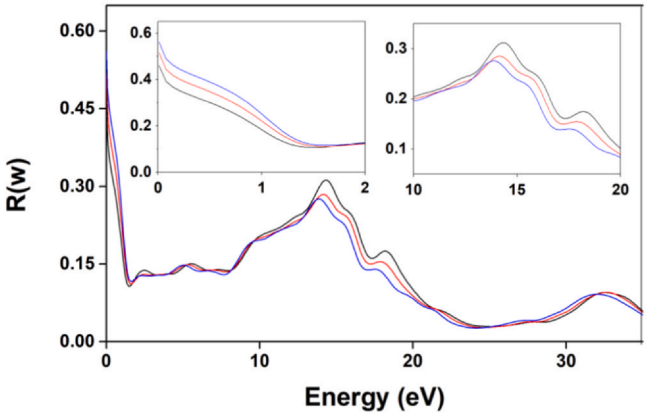

Fig. 11. Reflectivity related to photon energy. Left and right insets focus on a detailed picture of the Cd concentration-related behavior of reflectivity corresponding photon energy interval of 0–1 eV and 10–20 eV, respectively.

4. Conclusion

$Zn_{1-x}Cd_xO$(x = 0.01, 0.02, 0.03, 0.04, 0.05, 0.1, 0.2, and 0.3) NPs were prepared by the sol–gel method. Structural analysis and estimations of stress, strain, and crystallite size were investigated according to their concentration dependence. The concentration-dependent crystallite size (D), microstrain (ε), stress (σ) values were estimated by applying various forms of Williamson–Hall procedure, such as the UDM, USDM, and UDEDM, and those values were compared with the Scherrer formula. Statistical analysis showed that our model was very good for 5% of Cd, where the p-values were 0.0018, 0.0202, and 0.0061 for the UDM, USDM, and UDEDM, respectively. An X-ray diffraction analysis exhibited a single hexagonal ZnO structure up to 2% of Cd doping. After 2% of Cd, the secondary CdO phase appeared. By using the UDM, USDM, and UDEDM, the maximum particle sizes were found to be 49.36, 44.69, 47.07 nm at x = 0.05, and microstrain ε values were found to be 7, 4.1, and 5.62×10^{-4} at x = 0.05. Moreover, at x = 0.05, the maximum stresses σ were obtained with values of 60.4×10^6 and 81×10^6 N/m^2 using the USDM and UDEDM, respectively. The crystallite sizes oscillated as Cd concentration increased up to 5%, afterward crystallite size decreased as the doping ratio increased. Moreover, the oscillations in the stress and strain values might unveil

many physical imperfections and dislocations in the host lattice structure. These three models of the W–H analysis were supportive in calculating the strain, stress, crystallite size, and energy density values with a certain estimation, and therefore these models are highly attractive to describe the excellent crystal. Also, crystallite size showed a decrement trend for Cd amount of > 10% despite a random behavior that emerged for lower concentrations (Fig. 3). One can conclude that bandgap is decreased when crystallite size is reduced through increasing guest concentration. The DFT calculations within GGA and GGA+U based on experimental structural data deducing that high bandgap tuned via CBM instead of VB states and increasing Cd amount let bandgap lowered. A redshift was observed according to the absorption spectra of the visible region which is more obvious by increasing Cd amount.

CRediT authorship contribution statement

I already declared that the data was collected at Bahcesehir University Lab and I have got help with the programming codes regarding GGA-PBE calculations from Asst. Prof. Dr. Izzet Parug Duru whom I already acknowledged.

Declaration of Competing Interest

The authors declare that they have no known competing financial interests or personal relationships that could have appeared to influence the work reported in this paper.

Acknowledgments

The author is grateful for suggestions and comments made by the referees and thanks to Nanotechnology Lab staff members at Bahcesehir University-Istanbul, Turkey for their constructive comments and providing XRD, EDX, and SEM data, and Asst. Prof. Dr. Izzet Parug Duru for his help in GGA-PBE calculations. Computing resources used in this work were provided by the National Center for High-Performance Computing of Istanbul Technical University (UHeM), Turkey, under the grant number 1006342019.

Appendix A. Supporting information

Supplementary data associated with this article can be found in the online version at doi:10.1016/j.jallcom.2021.158620.

References

[1] S.P. Hoffmann, C. Meier, T. Zentgraf, W.-G. Schmidt, H. Herrmann, Zinc-Oxide-Based Photonic Crystal Membranes, University of Paderborn, 2018.
[2] A. Antony, P.P, I.V. Kityk, G. Myronchuk, G. Sanjeev, V.C. Petwal, V.P. Verma, J. Dwivedi, A study of 8MeV e-beam on localized defect states in ZnO nanostructures and its role on photoluminescence and third harmonic generation, J. Lumin. 207 (2019) 321–332.
[3] A. Sevik, B. Coskun, M. Soylu, The effect of molar ratio on the photo-generated charge activity of ZnO–CdO composites, Eur. Phys. J. 135 (2020) 65.
[4] F. Rahman, Zinc oxide light-emitting diodes: a review, Opt. Eng. 58 (1) (2019) 1.
[5] Y.-J. Noh, J.-G. Kim, S.-S. Kim, H.-K. Kim, S.-I. Na, Efficient semitransparent perovskite solar cells with a novel indium zinc tin oxide top electrode grown by linear facing target sputtering, J. Power Sources 437 (2019) 226894.
[6] D. Bremecker, P. Keil, M. Gehringer, D. Isaia, J. Rödel, T. Frömling, Mechanically tuned conductivity at individual grain boundaries in polycrystalline ZnO varistor ceramics, J. Appl. Phys. 127 (2020) 034101.
[7] K.P. Ghoderao, S.N. Jamble, R.B. Kale, Hydrothermally synthesized Cd-doped ZnO nanostructures with efficient sunlight-driven photocatalytic and antibacterial activity, J. Mater. Sci. Mater. Electron 30 (2019) 11208–11219.
[8] S.D. Senol, E. Ozugurlu, L. Arda, Synthesis, structure and optical properties of (Mn/Cu) co-doped ZnO nanoparticles, J. Alloy. Compd. 822 (2020) 153514.
[9] I.P. Duru, E. Ozugurlu, L. Arda, Size effect on magnetic properties of $Zn_{0.95-x}Mg_xNi_{0.05}O$ nanoparticles by Monte Carlo simulation, Ceram. Int. 45 (2019) 5259–5265.
[10] S.D. Senol, C. Boyraz, E. Ozugurlu, A. Gungor, L. Arda, Band gap engineering of Mg doped ZnO nanorods prepared by a hydrothermal method, Cryst. Res. Technol. 54 (3) (2019) 1800233.
[11] A. Guler, L. Arda, N. Dogan, C. Boyraz, E. Ozugurlu, The annealing effect on microstructure and ESR properties of (Cu/Ni) co-doped ZnO nanoparticles, Ceram. Int. 45 (2) (2019) 1737–1745.
[12] E. Mosquera, I. del Pozo, M. Morel, Structure and redshift of optical band gap in CdO–ZnO nanocomposite synthesized by the sol-gel method, J. Solid State Chem. 206 (2013) 265–271.
[13] N.M. Al-Hada, E. Saion, H.M. Kamari, M.H. Flaifel, A.H. Shaari, Z.A. Talib, N. Abdullahi, A.A. Baqer, A. Kharazmi, Structural, morphological and optical behavior of PVP capped binary $(ZnO)_{0.4}(CdO)0.6$ nanoparticles synthesized by a facile thermal route, Mater. Sci. Semicond. Process. 53 (2016) 56–65.
[14] N.M. Al-Hada, H.M. Kamari, C.A.C. Abdullah, E. Saion, A.H. Shaari, Z.A. Talib, K.A. Matori, Down-top nanofabrication of binary (CdO)x (ZnO)1–x nanoparticles and their antibacterial activity, Int. J. Nanomed. 12 (2017) 8309–8323.
[15] G. Somasundaram, J. Rajan, J. Paul, Effect of the calcination process on CdO–ZnO nanocomposites by a honey-assisted combustion method for antimicrobial performance, Toxicol. Res. 7 (2018) 779–791.
[16] M. Mahendiran, J.J. Mathen, M. Racik, J. Madhavan, M. Victor Antony Raj, Investigation of structural, optical, and electrical properties of transition metal oxide semiconductor CdOZnO nanocomposite and its effective role in the removal of water contaminants, J. Phys. Chem. Solids 126 (2019) 322–334.
[17] R. Liu, D. Zhao, L. Duan, X. Zhao, Optical and photocatalytic properties of Zn1-xCdxO nanoparticles with tuned oxygen vacancy, J. Alloy. Compd. 825 (2020) 153377.
[18] R. Santhi, C. Shanthi, M. Sathya, K. Pushpanathan, Self-assembled flower-like microstructure in Zn1−xCdxO nanoparticles, Trans. Nonferrous Met. Soc. China 27 (2017) 2031–2042.
[19] R. Yogamalar, R. Srinivasan, A. Vinu, K. Ariga, A.C. Bose, X-ray peak broadening analysis in ZnO nanoparticles, Solid State Commun. 149 (2009) 1919–1923.
[20] C. Boyraz, N. Dogan, L. Arda, Microstructure and magnetic behavior of (Mg/Ni) co-doped ZnO nanoparticles, Ceram. Int. 43 (17) (2017) 15986–15991.
[21] A.R. Stokes, A.J.C. Wilson, The diffraction of x rays by distorted crystal aggregates – I, Proc. Phys. Soc. 56 (3) (1944) 174–181.
[22] V.D.D. Mote, J.S.S. Dargad, Y. Purushotham, B.N.N. Dole, Effect of doping on structural, physical, morphological, and optical properties of $Zn_{1-x}Mn_xO$ nanoparticles, Ceram. Int. 41 (2015) 15153–15161.
[23] S.J. Clark, M.D. Segall, C.J. Pickard, P.J. Hasnip, M.J. Probert, K. Refson, M.C. Payne, First-principles methods using CASTEP, Z. Kristallogr. 220 (5–6) (2005) 567–570.
[24] J.P. Perdew, K. Burke, M. Ernzerhof, Generalized gradient approximation made simple, Phys. Rev. Lett. 77 (1996) 3865–3868.
[25] D.W. Boukhvalov, a I. Lichtenstein, V.V. Dobrovitski, M.I. Katsnelson, B.N. Harmon, V.V. Mazurenko, V.I. Anisimov, Effect of local Coulomb interactions on the electronic structure and exchange interactions in Mn12magnetic molecules, Phys. Rev. B 65 (2002) 184435.
[26] M.F.M. Taib, D.T. Mustaffa, N.H. Hussin, M.H. Samat, A.M.M. Ali, O.H. Hassan, M.Z.A. Yahya, First-principles study on Zn doped MgO using Hubbard U correction, Mater. Res. Express 6 (2019) 094012.
[27] I.P. Duru, E. Ozugurlu, L. Arda, A first-principles study of magnetic properties of $Zn_{0.94}Mg_{0.01}Mn_{0.05}O$, Mater. Res. Express 6 (2020) 126118.
[28] X.D. Zhang, M.L. Guo, W.X. Li, C.L. Liu, First-principles study of electronic and optical properties in wurtzite $Zn_{1-x}Cd_xO$, J. Appl. Phys. 103 (2008) 063721.
[29] R. Muhammad, Y. Shuai, H.-P. Tan, First-principles study on hydrogen adsorption on nitrogen-doped graphene, Phys. E 88 (2017) 115–124.
[30] B. Amin, M.I. Ahmad, S. Maqbool, G. Said, R. Ahmad, Ab initio study of the bandgap engineering of Al 1− x Ga x N for optoelectronic applications, J. Appl. Phys. 109 (2011) 023109.
[31] U.H. Bakhtiar, R. Ahmed, R. Khenata, M. Ahmed, R. Hussain, A first-principles comparative study of exchange and correlation potentials for ZnO, Mater. Sci. Semicond. Process. 16 (2013) 1162–1169.
[32] J. Lu, S. Fujita, T. Kawaharamura, H. Nishinaka, Y. Kamada, T. Ohshima, Z. Ye, Y. Zeng, Y. Zhang, L. Zhu, Carrier concentration dependence of band gap shift in n-type ZnO:Al films, J. Appl. Phys. 101 (8) (2007) 083705.
[33] S. Bai, S. Chen, Y. Zhao, T. Guo, R. Luo, D. Li, A. Chen, Gas sensing properties of Cd-doped ZnO nanofibers synthesized by the electrospinning method, J. Mater. Chem. A 2 (2014) 16697–16706.